

Amoeba-inspired swimming through isoperimetric modulation of body shape

Curtis Sparks¹, Nathan Justus², Ross Hatton², Nick Gravish¹, *Member, IEEE*,

Abstract—In this work we present the design of a swimming robot that is inspired by the body shape modulation of small microorganisms. Amoebas are small single celled organisms that locomote through deformation and shape change of their body. To achieve similar shape modulation for swimming propulsion in a robot we developed a novel flexible appendage using tape springs. A tape spring is an elongated strip of metal with a curved cross-section that can act as a stiff structure when loaded against the curvature, while it can easily buckle when loaded with the curvature. We develop a tape spring appendage that is capable of freely deforming its perimeter through two actuation inputs. In the first portion of this paper we develop the kinematics of the appendage mechanisms and compare with experiment. Next we present the design of a surface locomoting robot that uses two appendages for propulsion. From the appendage kinematics we derive the local connection vector field for locomotion kinematics and study the optimal gait for forward swimming. Lastly, we demonstrate robot swimming performance in open water conditions. The novel appendage design in this robot is advantageous because it enables omnidirectional movement, the appendages will not tangle in debris, and they are robust to collisions and contact with structures.

I. INTRODUCTION

Small robot platforms capable of locomotion on and below the surface have many applications in science and defense [1]. Recently there has been interest in small platforms that move through non-traditional locomotion methods such as bio-inspired propulsion [2], [3] (i.e. robots that do not use rotary propellers). Locomotion using appendages, undulatory surfaces, and fins have several advantages over propeller based locomotion including: 1) they will not tangle in debris as easily, 2) they can provide better control over force vectoring, and 3) they can provide multi-modal locomotion capabilities such as movement in confined environments or on dry land. In this paper we develop a surface swimming robot that uses a novel flexible appendage which is capable of quickly reconfiguring shape for propulsion. The appendages of this robot are inspired by the locomotion capabilities of small amoeboid swimming microorganisms.

Bio-inspired swimming robots have been developed that span many different locomotion modalities. Fish inspired robots comprise a broad range of sizes and morphologies, yet they typically use a common method of generating propulsion through oscillation of their body and fins [6]–[8]. Tuning the body and tail stiffness of these robots has lead to exceptional energetic efficiency during swimming [9]–[11].

¹School of Mechanical & Aerospace Engineering Department, University of California, San Diego. ²School of Mechanical Engineering Department, Oregon State University.
 Contact e-mail ngravish @eng.ucsd.edu

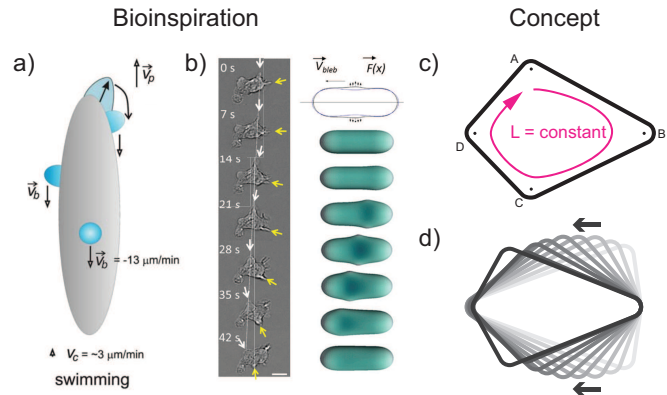


Fig. 1. a-b) Examples of swimming locomotion through body shape change in Amoebas. Images reproduced from [4] (a) and [5] (b). c-d) Robot locomotion concept. c) A body perimeter of constant length has four bends in it (A-D) that can be moved anywhere along the body perimeter. d) Example of a swimming stroke through shape modulation of a constant perimeter body.

However, robots that use a single tail fin for propulsion may lack maneuverability since there is little capability for generating thrust in directions different from the body axis (i.e. they can force vector). Similar force vectoring constraints are also present in robots that use jet propulsion, inspired from squid locomotion [12].

Robots that use two or multiple appendages or tentacles have demonstrated turning and force vectoring capabilities [13]–[16]. In this paper we take inspiration from the swimming of small amoeboid organism such as *dictyostelium discoideum*. Amoebas are microorganisms that don't have cell walls and thus can flexibly change the shape of their exterior body which enables locomotion. While amoebas are well known to move across substrates through body shape change, it has recently been shown that they can swim by producing protrusions on their body, called pseudopods, and propagating these down their body length to generate thrust [16], [17] (Fig. 1). To emulate this process we have developed and studied a novel mechanism based on tape springs for continuous shape change in swimming robot propulsion.

Tape springs are thin, curved strips of metal that are lightweight, directionally strong, and widely available. When a tape spring is bent opposite the curve it will buckle into a triangular shape in which two of the sides of the triangle have an unchanged cross-section and are stiff, while at the vertex of the triangle the tape follows a curved arc and the cross-section is flat (Fig. 2a) [18], [19]. At this “vertex” the bending stiffness is low, and furthermore the location of this

vertex can be easily moved along the length of the tape. By inducing a bend in a tape spring and then constraining the base length between the two ends, and one of the base angles, the tape spring can be actuated with kinematics similar to that of a prismatic-rotational-prismatic (PRP) system with a constant length requirement. Tape springs have been used in recently for self-deploying satellites because they can be compactly stored, as rolling hinges due to their low bending resistance, and for robot appendages and manipulators [20]–[25].

More broadly, nonlinear and anisotropic mechanisms are increasingly being incorporated into robotic systems because they can provide controlled energy release, hysteresis, and loading-dependent behavior. A common way to introduce nonlinearity and anisotropic behavior into robot mechanisms is through the presence of curvature in the constituent material that makes up the body or appendage. Curvature can induce structural stiffness (e.g., a paper tube versus a paper sheet), nonlinearity (e.g., through buckling), and anisotropy (e.g., through a tape spring with anisotropic stiffness). Furthermore, these mechanical behaviors can be reversed over many cycles when using elastic or inextensible materials and thus allow for reconfigurability of these mechanisms. Thus, we call robotics components formed from soft curved reconfigurable anisotropic mechanisms as SCRAMs. There is an increasing library of SCRAM mechanisms used in soft robotics including tubes that buckle to form local joints [26], [27], curved beams such as tape springs that buckle anisotropically [23], [25], curved tubes that propagate strain to distributed fins for locomotion [28], and laminate robot joints with variable stiffness [29], [30] and buckling to induce hysteresis [31].

This paper presents the Amoebot, a swimming robot that uses a pair of tape springs to propel itself through the water. The tape spring pair form a constant perimeter boundary that can undergo continuous shape change by actuating the base length and base angles of the tape springs. In section II of this paper we introduce the kinematics of the propulsion mechanism. Furthermore, we calculate the theoretical locomotor properties of this actuation method and we design a gait for optimal motor efficient forward swimming. In section III we present the design and fabrication details for our robot. Lastly, in section IV we present experimental results to study the kinematics of isolated tape springs, and the locomotion capabilities of the robot. We conclude with a discussion of the advantages and limitations of SCRAM based mechanisms for robot locomotion.

II. MODELING AND ANALYSIS OF AN ISOPERIMETRIC TAPE SPRING MECHANISM

In this section we develop the forward and inverse kinematics of the tape spring mechanism.

A. Inverse Kinematics

When a tape spring buckles it forms a triangular shape (Fig. 2a). The inverse kinematics of this system can be found using the triangular shape of the tape fin. A right triangle can

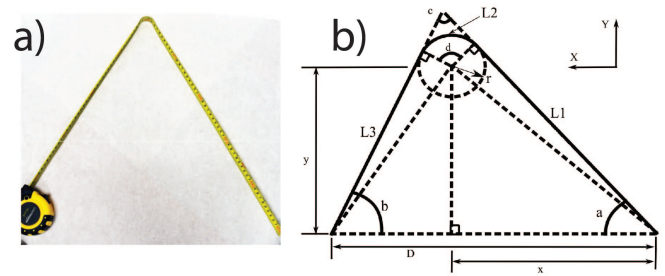


Fig. 2. a) Example of a tape spring with a single bend in the middle. b) Geometric modeling of the tape fin.

be drawn from the center of the curve's arc to the end point of the tape and the perpendicular line from the center point to the line between the two endpoints (Fig. 2b). The height of the right triangle formed is the y position of the center point and the base width of the triangle is the x position of the triangle. From there the hypotenuse of the right triangle and the sub-angle a_1 can be found. Another right triangle can be drawn using the straight part of the fin, the perpendicular radius of the arc and the line from the center to endpoint. The length from the center to the endpoint was found from the first triangle and the radius of the arc is assumed to be a known constant value. From these values, the length of the outer leg, L_1 , and the sub-angle, a_2 , can be calculated. The base angle a is found by combining a_1 and a_2 . Following a similar process on the other side of the fin, the length L_3 and angle b can be identified.

To find the length of the arc, L_2 , the triangular shape of the fin must be considered. Continuing the lines of the legs until they would meet, a larger triangle can be created. The imaginary angle at the tip of this triangle, c , must be $180^\circ - (a + b)$ due to the geometric properties of triangles. The angle of the arc, d , can then be found by considering the quadrilateral formed by the two radii and the imaginary lines from the legs to the top of the triangle. The angles of a quadrilateral must sum to 360° . The radii are perpendicular to the lines of the legs so they are 90° each. Combining these facts can set up the equation $d + 90^\circ + 90^\circ + (180^\circ - (a + b)) = 360^\circ$, and thus, $d = a + b$. The arc length L_2 is then $r d = r (a + b)$. Finally, combining the three section lengths L_1 , L_2 , and L_3 provides the total tape length L , and thus the angle and length of tape required to reach a given point.

B. Forward Kinematics

The forward kinematics of the system can be described with a set of vector equations. The shape of the triangle can be driven by a known total length of tape, L , one driving angle, a , and the length between the two endpoints, D . A vector can be drawn from the endpoint of the tape to the beginning of the curve. This vector has an unknown length L_1 , and forms a known angle, a , with the x axis. A second vector can be drawn from the end of the first vector to the center point of the arc. This second vector is perpendicular to the first and has a known length r , the radius of the arc. A similar set of vectors can be drawn for the opposite leg of the

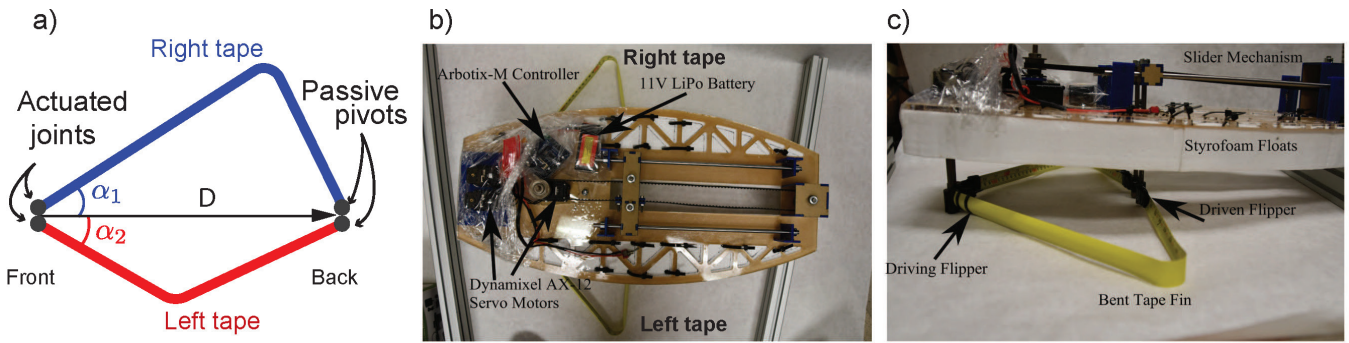


Fig. 3. a) Robot actuation concept. A left and a right tape spring comprise the propulsion surfaces. The left and right tapes have passive pivots at the front of the robot and individually actuated angles at the back of the robot. The length between front and back of the tapes is actuated and is the same for both left and right tape. b-c) Top and Side views showing driving components of the system.

fin. These two vector sets must both meet at the center point of the arc. This, combined with the limiting length equation, allows the creation of a set of equations that can be used to solve for the unknown lengths L_1 , L_2 , and the unknown angle b .

$$L_1 \cos(a) + r \cos(a - \frac{\pi}{2}) = D - (L_3 \cos(b) + r \cos(b - \frac{\pi}{2})) \quad (1)$$

$$L_1 \sin(a) + r \sin(a - \frac{\pi}{2}) = L_3 \sin(b) + r \quad (2)$$

$$\sin(b - \frac{\pi}{2})L_1 + L_3 + r(a + b) = L \quad (3)$$

These equations can be numerically solved in MATLAB. The x and y position can then be found.

$$x = L_1 \cos(a) + r \cos(a - \pi/2) \quad (4)$$

$$y = L_1 \sin(a) + r \sin(a - \pi/2) \quad (5)$$

III. ROBOT DESIGN

In our robot design we seek to exploit the properties of the tape spring to develop a propulsive appendage. The extensible properties of the tape allow for the creation of a long fin that can change its approximately triangular shape continuously by varying the base length of the triangle, and one of the base angles (Fig. 3a).

A swimming pattern can be created by manipulating the shape of the tape fin without changing its length, (Fig. 4). First the endpoints of the tape move closer together and extend the part of the tape that can move. Next changing the angle of the tape sweeps the fin back, pushing against the water. After pushing back, the endpoints of the tape are pushed further apart, shortening the fin. The angle of the tape is then reset but the shorter fin pushes against less water as the angle returns to the start. This pattern produces an uneven distribution of forces in which the fin pushes against more water on the backwards swing than it does on the forwards swing, and so propels the AmoeBot forward overall in each cycle.

The AmoeBot has a laser cut acrylic board for its base. Two Styrofoam blocks are attached to the underside of the acrylic base that enable the AmoeBot to float. The actuation

of each tape is driven by two sets of servo motors that control the base angles α_1 and α_2 . The motors are directly attached to a pair of shafts with a 3D printed flipper on the end which holds the end of the tapes. The length of the tapes endpoints is controlled by a slider mechanism on top of the board. A servo motor drives a belt which moves a slider box along a pair of oiled rails. The slider box holds two shafts which are free to rotate and have a 3D printed flipper on the end holding the other end of the tape. The shafts in the front of the AmoeBot are fixed to the motors and control the front angle of the tape fin. The shafts in the back are free to rotate. An Arbotix-M robocontroller is used to direct the motion of the three servo motors. The system is powered by an 11V LiPo battery.

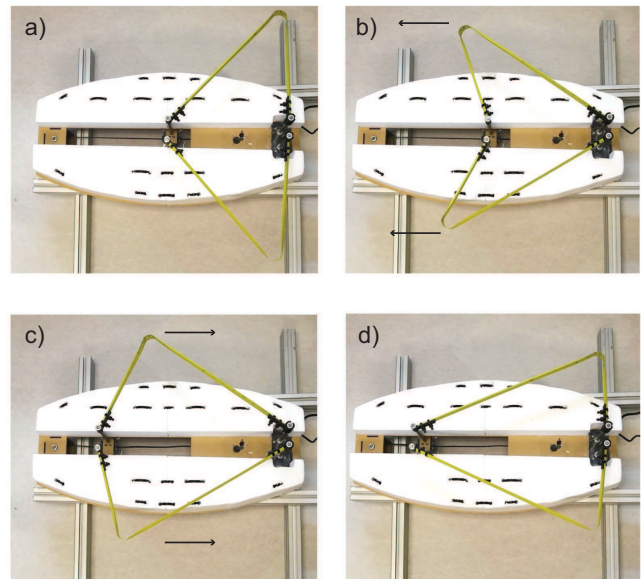


Fig. 4. Swimming Pattern of AmoeBot. a) Fins fully extended. b) Fins swept backwards to push against water. c) Fins shortened by extending base distance. d) Angle of fins reset to original, ready to extend and repeat pattern.

IV. RESULTS

Here we report results from modeling and experimental analysis of the tape spring actuation mechanisms and our robot. In the first section we validate the kinematic modeling of the tape mechanism. Next we study the optimal gaits for forward locomotion in this robot using methods from geometric mechanics. Lastly, we report results from constrained and free-swimming experiments with the full robot.

A. Tape spring kinematics

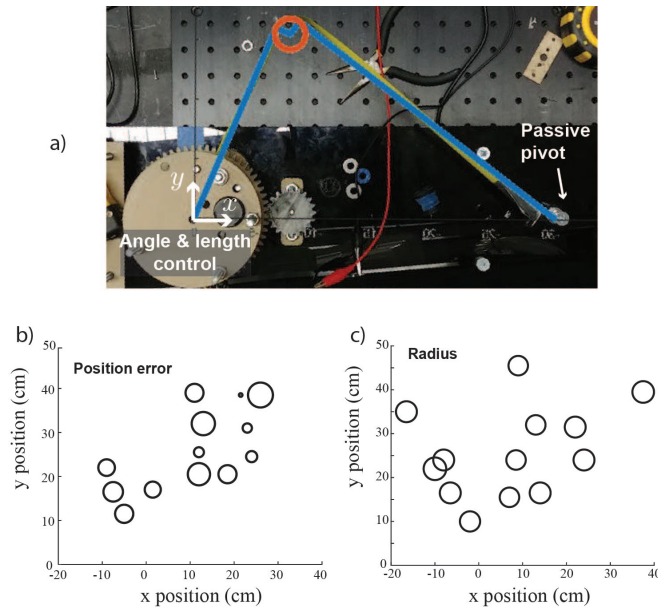


Fig. 5. Experiment to measure the kinematics and constant radius assumption of the tape spring bend. a) Experimental setup overlaid with model prediction b) position error denoted by marker size at different locations in the workspace. c) Radius of the bend denoted by marker size at different locations in the workspace.

The kinematic models were tested using a setup with a rotating platform and motorized pair of wheels shaped to match the curve of the tape (Fig. 5). The pair of wheels were in contact with the tape such that when the driving wheel turned, the tape was extended or retracted. The pair of wheels was mounted on the rotating platform offset from the center. When the platform turned it would change the angle of the wheels relative to the center of the platform. As the tape extends straight out from the paired wheels, changing the angle of the wheels would change the angle of the tape. A coordinate system was used where the X axis was the direction from the driving endpoint to the driven endpoint and the Y axis points outward in the direction of fin extension perpendicular to the X axis (Top Fig. 5). The point being measured for position was the center of the curve at the rolling joint of the tape fin.

To test the forwards kinematics, the model's predictions for a given angle and length are compared to the measured position. The tape fin was driven to a chosen tape length and angle with the testing platform. The X and Y location were measured using a second tape measure. The tape measure

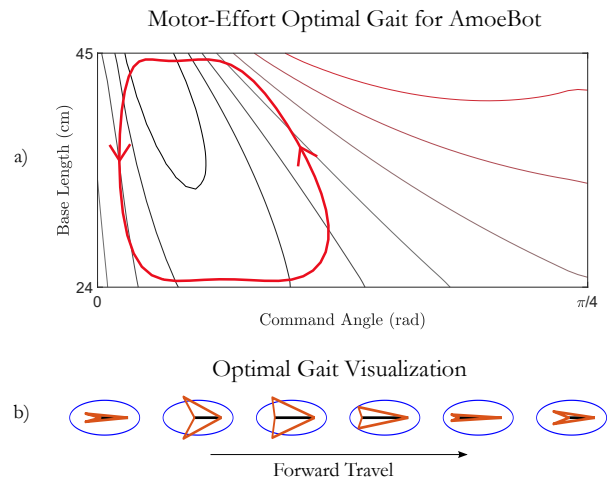


Fig. 6. Estimated motor-force optimal gait for AmoeBot. a) Optimal gait (red path) superimposed on the forward-travel CCF for AmoeBot. Enclosing black high-value regions of the CCF promotes longer forward travel per cycle. b) Illustration of the optimal gait as it progresses through the motion. Gait images are uniformly separated to visualize swimmer shape at each point in the gait.

was held perpendicular to the platform with a carpenter's square and the distance from the edge of the platform to the center of the radius was measured, giving the Y value. Then the distance from the rotating joint to the square was measured giving the X value. The chosen angle and length were then fed into the forward kinematic models running in MATLAB. The resulting prediction was then compared to the measured value. The average X error was 1.4cm and the average Y error was 0.74cm. The average percent error for X and Y was 5.9% and 4.1% respectively.

A similar test was used for the inverse kinematics. The system was driven to a series of X, Y positions. The X and Y position was measured and the tape angle and length were recorded. The X and Y positions were then fed into the inverse kinematics model running in MATLAB which would return a predicted angle and length. The predicted and measured length and angle were then compared (Fig. 5 middle). The average angle error was 2.4° and average length error was 0.8cm. The average percent error was 3% and the average length error was 1.4%.

The assumption of a constant radius at the rolling joint was also evaluated. The tape fin was driven to various positions, and the X and Y location was recorded using the method described above. Then a cylinder of adjustable radius consisting of a rolled up piece of plastic sheet was placed into the joint and then expanded until its radius matched that of the joint. The diameter of the cylinder was then measured with a tape measure (Fig. 5 bottom). The average radius of the joint was found to be 1.5cm. The joint did change in size, with a standard deviation of 0.1cm. However this change was not large enough to greatly affect the kinematic modeling.

B. Modeling Locomotion

To estimate the locomotive behavior of the AmoeBot, we approximate each fin as a combination of two flat hydrodynamic plates representing the straight lengths of tape. The instantaneous lengths and orientations of these idealized plates in the fluid are functions of our shape parameters, the commanded angle α_i and commanded base distance D shown in Fig. 3a. Using flat plate theory, we can estimate the principal mass and added mass matrix μ for each of the four total hydrodynamic elements that compose the two fins of the AmoeBot. An additional mass component was added that represents the hydrodynamic mass of the buoyant platform and all other robotic elements attached to it that do not move with respect to the platform.

By establishing the x and y coordinates of the midpoint of each plate as a function of our shape parameters, derivatives of these midpoints can be taken with respect to the shape variables and used to compose the mobile Jacobian for each fin element in water. This Jacobian provides a mapping of the velocity of the AmoeBot in its local body coordinates \mathring{g} and the variable velocities $\dot{\alpha}$ and \dot{D} to the velocity of the fin element through the water. These Jacobians specifically provide the relationship

$$v_i = J_i(\alpha, D) \begin{bmatrix} \mathring{g} \\ \dot{\alpha} \\ \dot{D} \end{bmatrix} \quad (6)$$

where v_i represents the velocity in the fluid of the i th fin element in the same local axes as the element's principal hydrodynamic mass matrix. With these Jacobians, we can pull back each fluid mass element onto the body frame of the AmoeBot and sum to get the total hydrodynamic mass matrix as a function of the shape variables:

$$M(\alpha, D) = \sum_i J_i^T(\alpha, D) \mu_i J_i(\alpha, D) \quad (7)$$

We can then use geometric techniques as laid out in [32] to estimate the AmoeBot's locomotive behavior from the properties of this total mass matrix and to examine what a useful 'gait' in the shape-space of the AmoeBot might look like. One especially useful component of these geometric techniques is the constraint curvature field (CCF). The CCF quantifies approximately how much locomotion in a given direction is gained by enclosing a certain region of the shape-space with a gait. Good gaits enclose high-value regions of the CCF while avoiding oppositely-signed areas. The CCF also allows for convenient optimization of gait locomotion with respect to a given cost function. For the AmoeBot, our cost function was the power dissipated by the actuators such that a good gait will minimally tax the motors. The AmoeBot gait optimized on the forward-travel CCF with respect to motor-effort is overlaid on the CCF in Figure 6(a), and an illustration of the resulting optimal gait can be seen below in Figure 6(b).

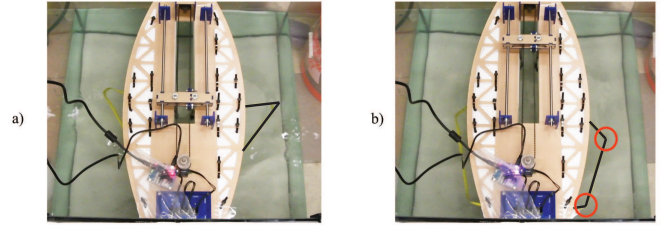


Fig. 7. Formation of secondary kinks during middle of return stroke. a) During the backstroke the fin remains rigid. b) During the return stroke a second buckling occurs as the fin resets. The two buckling joints are marked with red circles.

C. Gait generation testing

We implemented an approximation to the optimal gait in the AmoeBot robot by varying the tape base length D over the range 30 cm to 45 cm, and the base angles $\alpha_1 = \alpha_2$ over the range 30° to 90° . The gait used in experiment is shown in Figure 4 from the underside of the robot. The gait begins in position 4a with the fins fully extended. The angle of the fins is then swept back to position 4b pushing against the water and propelling the AmoeBot forwards. The fins are then shortened by lengthening the distance D to 4c. The angle is then swept forwards with the shorter fins to 4d. Finally the fins are returned to their original length by shortening D and resuming the starting position 4a.

To ensure that the tapes could withstand the force of pushing against the water without buckling, the AmoeBot was placed in a small tank filled with water and driven through its swimming pattern while held stationary. On the backwards push stroke the fin maintained its shape and pushed against the water as expected. However, on the forwards stroke an unexpected second buckling of the tape occurred as it reset to the starting position as shown in Figure 7. The initial tests were conducted with a speed limit of 90rpm for the angle driving motors. This speed limit was lowered in steps of 10rpm until the second buckling no longer occurred. The extra buckling stopped happening when the speed limit was lowered to 20rpm. The unexpected buckling breaks the kinematic model, but does not impede the swimming motion.

A second test was conducted in the small tank to see how the fins interact with obstructions. With the AmoeBot held stationary in the tank, plastic seaweed was placed around the fins. The fins were then driven back and forth through the seaweed as shown in Figure 8. On the backwards stroke the fin pushed through the obstructing seaweed. On the return forwards stroke the fin bent around obstructions that it could not sweep past. This behavior shows that there may be advantages using tape fins in heavily obstructed or weeded water as it can push through and bend around seaweed that would tangle up in a rotary propeller.

D. Unconstrained motion testing

The Amoebot was tested in open water in a large swimming pool. Foot long increments were marked on the side of the pool. There were two cameras set up to record the motion of the Amoebot. The first was a camera placed off the side of the pool watching the Amoebot and distance markers. The second was mounted on a drone and recorded the overhead view of the motion shown in the top of Figure 9. The Amoebot was placed in the pool, turned on and released. The two cameras recorded its motion as it moved. From these recordings the speed of motion was measured to be 0.15 feet per second.

In the first attempts at swimming the Amoebot generated successful forward trajectories and was able to move across the pool. During these trials the robot orientation was uncontrolled and due to asymmetries in the robot, as well as wind from the surface, the robot orientation drifted. After several experiments the robot began to decrease in performance. The joint connecting the motors to the driving shafts and flippers began to fail, resulting in mis-alignment of the tape fins. This mis-alignment resulted in the unsuccessful trajectories where the Amoebot was unable to move across the water and instead remained mostly stationary. This test proved that the Amoebot is capable of producing forward movement, although more work is required to make the system more robust and reliable.

E. Swimming Measurements

The effect of changing the angle on the forward movement of the swimming pattern was tested. The driving tape fins were strengthened by using two tape springs set with opposite curvature held together inside a sleeve of heat sealed fabric. These strengthened fins were more resistant to the double buckling that occurred with the previous design. With the new fins attached, the Amoebot was placed in a small outdoor pool. A camera was placed looking down on the pool from above. The Amoebot was run through four cycles of the swimming pattern while the camera recorded video. The sweeping angle of the Amoebot movement pattern is the decrease in the control angle α from 90 degrees to the minimum angle of the pattern. The sweeping angle was varied from 10 to 70 degrees. The distance moved in each cycle of the swimming pattern was measured from the video recordings and the average distance per cycle was recorded. As the sweeping angle of the pattern increases from 10 to 70 degrees, the distance moved in each cycle increased as shown

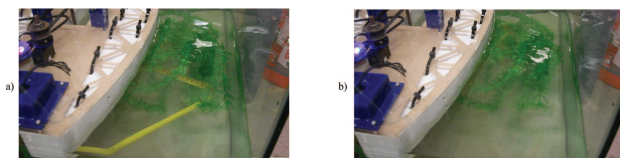


Fig. 8. Tape Fin passing through a seaweed like obstruction. a) On the swing forwards, the tape buckles and bends around obstructions. b) On the swing backwards, the tape pushes through the obstructing seaweed without buckling.

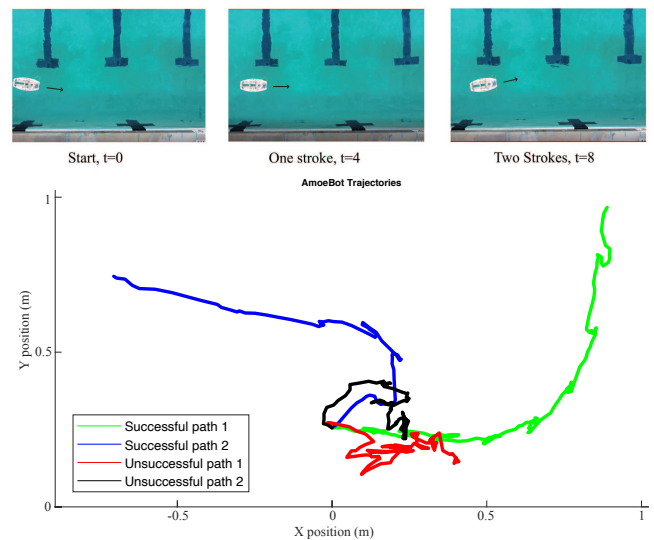


Fig. 9. Open water swimming experiments were performed (top). Examples of swimming can be seen in supplementary video. Swimming trajectories of the Amoebot moving in open water are shown in bottom plot. The green and blue trajectories show successful motion across the pool's surface. The black and red trajectories are failed attempts at motion.

in Figure 10. The cycle was also attempted at a sweep angle of 80 degrees, but one of the strengthened tape fins began to exhibit the double buckling behavior.

The turning capabilities of the Amoebot were also tested. Similar to the forward tests, the Amoebot was placed in a small outdoor pool with a camera looking down. For each turning test, one of the two fins was driven through the normal swimming pattern. The other fin was held stationary at $\alpha = 90^\circ$. The sweep angle difference is the sweep angle of the right fin minus the sweep angle of the left fin. The Amoebot was run through three turning cycles for each test and the average turn per cycle was recorded. The rotation measured is defined around the positive z axis

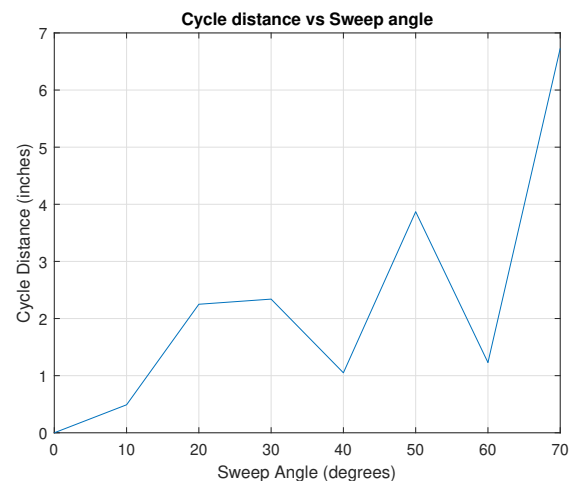


Fig. 10. Average distance moved per cycle as depends upon the sweep angle of the Amoebot motion pattern.

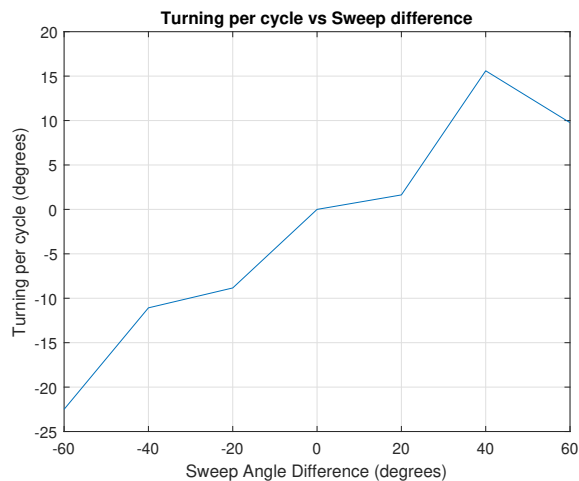


Fig. 11. Angle turned per cycle in degrees as depends upon the sweep angle difference of the Amoebot turning pattern, where one fin is held stationary while the other rotates.

coming vertically upwards from the pool surface. When only one fin is moved, the Amoebot will turn in the opposite direction as shown in Figure 11. When the sweep difference is positive, and only the right fin is moving, the Amoebot will turn to the left. When the sweep difference is negative, and only the left fin is moving, the Amoebot will turn to the right. The angle turned with each cycle also increases as the magnitude of the sweep angle increases.

V. DISCUSSION AND CONCLUSION

the Amoebot was designed to mimic the motion of an amoeba, using the continuous shape change of an isoperimetric pair of fins formed from tape springs. This gives advantages in obstructed waters where seaweed or other obstacles may make traversal difficult for propeller based locomotion. Furthermore, the appendages could be used to brace against nearby objects to potentially hold position in water currents. The anisotropic stiffness of the tape springs provides enough strength to push through the water with a lightweight arm while remaining easy to manipulate.

A pair of models, one for forwards kinematics and one for backwards kinematics were created to describe the motion of the fin formed by bending the tape spring. The models show that the position of the fin can be completely described by the length of the tape, the distance between the endpoints, and one driving angle. This allows for planar control and positioning of the tape fin similar to that of a PRP system. By locking the tape length, the shape of the isoperimetric fin is fully described with just the endpoint distance and driven angle.

The developed kinematic models were compared to the empirical performance using a testing platform with a fixed endpoint distance and control over tape length and driving angle. The models were able to successfully predict both the position of the fin at a given angle and length, and the required angle and length values to reach a given point.

Following previous methods developed for low Reynolds number swimming [33], and later updated for inertial swimming [32] we computed the optimal gait of the robot. A simplified version of this gait was implemented in the robot and was tested in constrained and unconstrained experiments. The Amoebot showed in small tank tests that the tape fins were capable of withstanding the forces required to push against the water and propel itself. It also showed that the tapes were capable of pushing through or bending around obstructions like seaweed that might make traversal through obstructed waters difficult. In swimming pool tests the Amoebot showed that it was capable of moving across the surface of the water propelled only by its tape fins and simple on-board controls.

This method of actuation presents promise for novel bio-inspired swimming robots. While the tape spring exhibited anomalous buckling which degraded performance this can be improved in future designs through modified springs that use stiffer constituent materials. An advantage of using the tape spring based actuation is that it will enable more omnidirectional movement than typical propeller based robots. The geometric methods developed for optimal gaits [32], [33] further will enable us to explore optimal control of swimming trajectories.

ACKNOWLEDGMENTS

Funding support was provided through the Mechanical and Aerospace Engineering Department at UCSD. This material is based upon work supported by the National Science Foundation under Grant No. 1935324. Any opinions, findings, and conclusions or recommendations expressed in this material are those of the author(s) and do not necessarily reflect the views of the National Science Foundation. Arnav Wyade assisted with the turning and cycle distance experiments.

REFERENCES

- [1] T. B. Curtin, D. M. Crimmins, J. Curcio, M. Benjamin, and C. Roper, "Autonomous underwater vehicles: trends and transformations," *Mar. Technol. Soc. J.*, vol. 39, no. 3, 2005.
- [2] D. T. Roper, S. Sharma, R. Sutton, and P. Culverhouse, "A review of developments towards biologically inspired propulsion systems for autonomous underwater vehicles," *Proc. Inst. Mech. Eng. Part M: J. Eng. Marit. Environ.*, vol. 225, no. 2, pp. 77–96, May 2011.
- [3] R. Salazar, A. Campos, V. Fuentes, and A. Abdelkefi, "A review on the modeling, materials, and actuators of aquatic unmanned vehicles," *Ocean Eng.*, vol. 172, pp. 257–285, Jan. 2019.
- [4] P. J. M. Van Haastert, "Amoeboid cells use protrusions for walking, gliding and swimming," *PLoS One*, vol. 6, no. 11, p. e27532, Nov. 2011.
- [5] L. Aoun, A. Farutin, N. Garcia-Seyda, P. Nègre, M. S. Rizvi, S. Tlili, S. Song, X. Luo, M. Biarnes-Pelicot, R. Galland, J.-B. Sibarita, A. Michelot, C. Hivroz, S. Rafai, M.-P. Valignat, C. Misbah, and O. Theodoly, "Amoeboid swimming is propelled by molecular paddling in lymphocytes," *Biophys. J.*, vol. 119, no. 6, pp. 1157–1177, Sep. 2020.
- [6] A. D. Marchese, C. D. Onal, and D. Rus, "Autonomous soft robotic fish capable of escape maneuvers using fluidic elastomer actuators," *Soft Robot*, vol. 1, no. 1, pp. 75–87, Mar. 2014.
- [7] T. Li, G. Li, Y. Liang, T. Cheng, J. Dai, X. Yang, B. Liu, Z. Zeng, Z. Huang, Y. Luo, T. Xie, and W. Yang, "Fast-moving soft electronic fish," *Sci Adv*, vol. 3, no. 4, p. e1602045, Apr. 2017.
- [8] A. Raj and A. Thakur, "Fish-inspired robots: design, sensing, actuation, and autonomy—a review of research," *Bioinspir. Biomim.*, vol. 11, no. 3, p. 031001, Apr. 2016.

- [9] C. J. Esposito, J. L. Tangorra, B. E. Flammang, and G. V. Lauder, "A robotic fish caudal fin: effects of stiffness and motor program on locomotor performance," *J. Exp. Biol.*, vol. 215, no. 1, pp. 56–67, 2012.
- [10] Q. Zhong, J. Zhu, F. E. Fish, S. J. Kerr, A. M. Downs, H. Bart-Smith, and D. B. Quinn, "Tunable stiffness enables fast and efficient swimming in fish-like robots," *Science Robotics*, vol. 6, no. 57, Aug. 2021.
- [11] J. Shintake, V. Cacucciolo, H. Shea, and D. Floreano, "Soft biomimetic fish robot made of dielectric elastomer actuators," *Soft Robot*, vol. 5, no. 4, pp. 466–474, Aug. 2018.
- [12] T. Bujard, F. Giorgio-Serchi, and G. D. Weymouth, "A resonant squid-inspired robot unlocks biological propulsive efficiency," *Sci Robot*, vol. 6, no. 50, Jan. 2021.
- [13] A. Villanueva, C. Smith, and S. Priya, "A biomimetic robotic jellyfish (robojelly) actuated by shape memory alloy composite actuators," *Bioinspir. Biomim.*, vol. 6, no. 3, p. 036004, Sep. 2011.
- [14] S.-W. Yeom and I.-K. Oh, "A biomimetic jellyfish robot based on ionic polymer metal composite actuators," *Smart Mater. Struct.*, vol. 18, no. 8, p. 085002, Jun. 2009.
- [15] H. Godaba, J. Li, Y. Wang, and J. Zhu, "A soft jellyfish robot driven by a dielectric elastomer actuator," *IEEE Robotics and Automation Letters*, vol. 1, no. 2, pp. 624–631, Jul. 2016.
- [16] M. Sfakiotakis, A. Kazakidi, A. Chatzidaki, T. Evdaimon, and D. P. Tsakiris, "Multi-arm robotic swimming with octopus-inspired compliant web," in *2014 IEEE/RSJ International Conference on Intelligent Robots and Systems*, Sep. 2014, pp. 302–308.
- [17] E. J. Campbell and P. Bagchi, "A computational model of amoeboid cell swimming," *Phys. Fluids*, vol. 29, no. 10, p. 101902, Oct. 2017.
- [18] K. A. Seffen and S. Pellegrino, "Deployment dynamics of tape springs," *Proceedings of the Royal Society of London. Series A: Mathematical, Physical and Engineering Sciences*, vol. 455, no. 1983, pp. 1003–1048, Mar. 1999.
- [19] H. Yang, R. Liu, Y. Wang, Z. Deng, and H. Guo, "Experiment and multiobjective optimization design of tape-spring hinges," *Struct. Multidiscip. Optim.*, vol. 51, no. 6, pp. 1373–1384, Jun. 2015.
- [20] O. G. Osele, A. M. Okamura, and B. H. Do, "A lightweight, High-Extension, planar 3-Degree-of-Freedom manipulator using pinched bistable tapes," in *2022 International Conference on Robotics and Automation (ICRA)*, May 2022, pp. 1190–1196.
- [21] J. Zhang, A. Song, X. Xu, and W. Lu, "A rigid and flexible structures combined deployable boom for space exploration," in *2016 IEEE/RSJ International Conference on Intelligent Robots and Systems (IROS)*, Oct. 2016, pp. 2920–2926.
- [22] D. Piovesan, M. Zaccariotto, C. Bettanini, M. Pertile, and S. Debei, "Design and validation of a Carbon-Fiber collapsible hinge for space applications: A deployable boom," *J. Mech. Robot.*, vol. 8, no. 3, Mar. 2016.
- [23] M. Sharifzadeh and D. Aukes, "Curvature-Induced buckling for Flapping-Wing vehicles," *IEEE/ASME Trans. Mechatron.*, pp. 1–1, 2020.
- [24] T. G. Chen, B. Miller, C. Winston, S. Schneider, A. Bylard, M. Pavone, and M. R. Cutkosky, "ReachBot: A small robot with exceptional reach for rough terrain," in *2022 International Conference on Robotics and Automation (ICRA)*, May 2022, pp. 4517–4523.
- [25] M. Sharifzadeh, Y. Jiang, and D. M. Aukes, "Reconfigurable curved beams for selectable swimming gaits in an underwater robot," *IEEE Robotics and Automation Letters*, vol. 6, no. 2, pp. 3437–3444, Apr. 2021.
- [26] Y. Jiang, M. Sharifzadeh, and D. M. Aukes, "Reconfigurable soft flexure hinges via pinched tubes," in *2020 IEEE/RSJ International Conference on Intelligent Robots and Systems (IROS)*, Oct. 2020, pp. 8843–8850.
- [27] M. Jiang, Q. Yu, and N. Gravish, "Vacuum induced tube pinching enables reconfigurable flexure joints with controllable bend axis and stiffness," in *2021 IEEE 4th International Conference on Soft Robotics (RoboSoft)*, Apr. 2021, pp. 315–320.
- [28] Y. Jiang, M. Sharifzadeh, and D. M. Aukes, "Shape change propagation through soft curved materials for Dynamically-Tuned paddling robots," in *2021 IEEE 4th International Conference on Soft Robotics (RoboSoft)*, Apr. 2021, pp. 230–237.
- [29] M. Jiang and N. Gravish, "Reconfigurable laminates enable multifunctional robotic building blocks," *Smart Mater. Struct.*, vol. 30, no. 3, p. 035005, Mar. 2021.
- [30] —, "Sliding-Layer laminates: A robotic material enabling robust and adaptable undulatory locomotion," in *2018 IEEE/RSJ International Conference on Intelligent Robots and Systems (IROS)*, Oct. 2018, pp. 5944–5951.
- [31] M. Jiang, R. Song, and N. Gravish, "Knuckles that buckle: compliant underactuated limbs with joint hysteresis enable minimalist terrestrial robots," in *2020 IEEE/RSJ International Conference on Intelligent Robots and Systems (IROS)*, Oct. 2020, pp. 3732–3738.
- [32] R. L. Hatton, Z. Brock, S. Chen, H. Choset, H. Faraji, R. Fu, N. Justus, and S. Ramasamy, "The geometry of optimal gaits for inertia-dominated kinematic systems," Jan. 2021.
- [33] R. L. Hatton and H. Choset, "Geometric motion planning: The local connection, stokes' theorem, and the importance of coordinate choice," *Int. J. Rob. Res.*, vol. 30, no. 8, pp. 988–1014, Jul. 2011.